PHYSICAL REVIEW B **108**, 024419 (2023)

Field-free spin-orbit torque switching and large dampinglike spin-orbit torque efficiency in synthetic antiferromagnetic systems using interfacial Dzyaloshinskii-Moriya interaction

Yoshiaki Saito,[1,*] Shoji Ikeda,[1,2,3,4] Nobuki Tezuka,[2,5] Hirofumi Inoue,[1] and Tetsuo Endoh[1,2,3,4,6]
[1] *Center for Innovative Integrated Electronic Systems, Tohoku University, Sendai 980-0845, Japan*
[2] *Center for Spintronics Research Network, Tohoku University, Sendai 980-8577, Japan*
[3] *Center for Science and Innovation in Spintronics, Tohoku University, Sendai 980-8577, Japan*
[4] *Research Institute of Electrical Communication, Tohoku University, Sendai 980-8577, Japan*
[5] *Department of Materials Science, Graduate School of Engineering, Tohoku University, Sendai 980-8579, Japan*
[6] *Department of Electrical Engineering, Graduate School of Engineering, Tohoku University, Sendai 980-8579, Japan*

(Received 25 April 2023; revised 26 June 2023; accepted 11 July 2023; published 20 July 2023)

Deterministic switching of perpendicularly magnetized systems using spin-orbit torque (SOT) usually requires an in-plane auxiliary magnetic field, which limits its practical applications. Here, an interfacial Dzyaloshinskii-Moriya interaction is introduced into perpendicularly magnetized synthetic antiferromagnetic (AFM) systems by changing the type of capping or underlayer in the [capping layer]/Co/[Pt/Ir/Pt spacer layer]/Co/[underlayer] synthetic AFM system. Field-free switching in the synthetic AFM system is observed in the cases of W, Ta, $Ir_{22}Mn_{78}$ capping layers or $Ir_{22}Mn_{78}$ underlayer. Among the synthetic AFM systems with field-free switching, the synthetic AFM system with $Ir_{22}Mn_{78}$ capping layer shows the largest dampinglike SOT efficiency, $\xi_{DL} = 28.1\%$. We also found observed large ξ_{DL} is related to the enhancement of spin absorption in antiferromagnetic Co magnetization configuration in synthetic AFM system compared to that in ferromagnetic Co magnetization configuration and the degree of enhancement increases with increasing the magnitude of interlayer exchange coupling between Co layers in synthetic AFM system. These results suggest that the synthetic AFM system is a promising building block for future nonvolatile high-speed memories and logic circuits using the spin Hall effect.

DOI: 10.1103/PhysRevB.108.024419

I. INTRODUCTION

In recent years, spin-orbit torque (SOT) originating from the spin-Hall effect (SHE) has aroused extensive interest among researchers due to their potential applications for SOT-magnetoresistive random-access memory (MRAM), skyrmion and domain wall devices [1–23]. However, there is a major challenge in realizing high-performance SOT devices. The challenge is that perpendicular magnetization is difficult to achieve SOT switching without an external magnetic field, while the use of perpendicular magnetization devices such as magnetic tunnel junctions with ferromagnetic electrodes possessing a perpendicular magnetic easy axis [24] is essential for achieving high-density memory. The spin orientation of the generated spin current from SHE is orthogonal to the out-of-plane direction, thus it cannot switch the perpendicular magnetization deterministically. To solve this problem, assistance from an in-plane external magnetic field (H_{ex}) has frequently been used to break the in-plane symmetry [1,6].

SOT switching of perpendicularly magnetized synthetic antiferromagnetic (AFM) systems has been reported in various systems [22,25–30], however, such switching also requires an additional in-plane magnetic field to break the inversion symmetry. Up to now, the field-free SOT switching of perpendicular synthetic AFM system is only realized through adjusting the domain wall configuration between Bloch type and Néel type [31] and introducing an in-plane exchange bias [32], exchange field gradient [33], and Dzyaloshinskii-Moriya (DM) interaction [34–36] in the various synthetic AFM systems. Although those methods advance partially for SOT-based synthetic AFM systems toward real applications, any new approaches for simultaneous achieving of field-free switching and high SOT efficiency are highly necessary and worthy of deep and systematic investigations. Also, most of the experimental studies in synthetic AFM systems used wedge structures in their films [31,33,34] or deposition method in an in-plane magnetic field [35] for introducing interlayer DM interaction [35,37] to obtain field-free switching, and in the case of using the interfacial DM interaction [38,39], complex multiple transitions of switching orientations between clockwise and anticlockwise near zero field were observed [34,36]. Therefore, these methods are not always beneficial to applications.

In this study, we conducted systematic experiments aiming to simultaneously achieve field-free switching and high SOT efficiency using the interfacial DM interaction. The reason for observing the complex multiple transitions of switching orientations between clockwise and anticlockwise near zero field in synthetic AFM systems [34,36] is due to the DM interaction acting on the top and bottom ferromagnetic layers in the synthetic AFM structure. The Landau-Lifshitz-Gilbert (LLG) simulation [34] shows that magnitude of the deterministic SOT critical switching field in synthetic AFM structure

---

[*] yoshiaki.saito.d7@tohoku.ac.jp

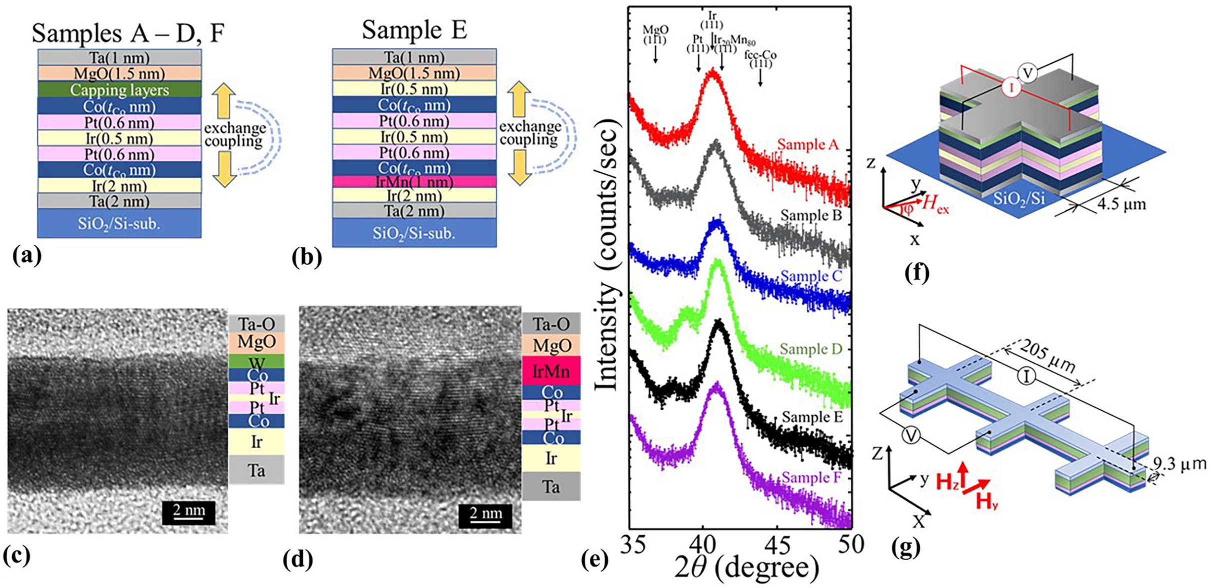

FIG. 1. (a), (b) Schematic of prepared film structures for Samples A-F in Table I. (c), (d) Cross-sectional transmission electron microscopy images in the synthetic AFM layers with W capping layer (Sample A) and $Ir_{22}Mn_{78}$ capping layer (Sample D), respectively. (e) Results of x-ray diffraction (XRD) measurements for Samples A−F. Typical device images and the measurement configurations for (f) the Hall bar and (g) spin Hall magnetoresistance measurements.

increases with increasing strength of the DM interaction field (H_{DM}) acting simultaneously on the top and bottom ferromagnetic layers in the synthetic AFM systems, and shows that deterministic SOT critical switching field is mainly determined by the weaker one of the top and bottom H_{DM}. Therefore, for a practical application of the synthetic AFM system, one of the top and bottom H_{DM} should be as small as possible. Recently, we found that the magnitude of the interfacial DM interaction is very small for the Pt/Co/Ir structures [22], because the DM interaction at the interface of Co and Ir is the similar magnitude to that of the Co and Pt, and the Pt/Co interface and Ir/Co interface possess the same sign [22,40–45]. Therefore, we used an Ir layer as either the capping or underlayer for the Co layer in the synthetic AFM system in the [capping layer]/Co/[Pt/Ir/Pt spacer layer]/Co/[underlayer] structure. We tried to change another underlayer or capping layer material in order to change the magnitude of H_{DM} for another Co layer in the synthetic AFM system.

II. EXPERIMENTAL PROCEDURE

We investigated SHE in synthetic AFM systems consisting of [capping layer]/Co/[Pt/Ir/Pt]/Co/[Ir underlayer]/Ta [Fig. 1(a)] and [Ir capping layer]/Co/[Pt/Ir/Pt]/Co/[$Ir_{22}Mn_{78}$ underlayer]/Ir/Ta [Fig. 1(b)]. All stack structures in this study are prepared on thermally oxidized Si substrates by RF sputtering on rotating substrates at room temperature. Detailed film structures are shown in Table I. In this study, we propose the synthetic AFM system in which one Co layer has a weak interfacial DM interaction and the other Co layer has a relatively large interfacial DM interaction. We use the Pt/Co/Ir structure for the one Co layer interface with a weak interfacial DM interaction [22,40–45]. In order to change the magnitude of H_{DM}, we investigated W/Co/Pt (Sample A with W capping layer), Ta/Co/Pt (Sample B with Ta capping layer), Mo/Co/Pt (Sample C with Mo capping layer), $Ir_{22}Mn_{78}$/Co/Pt (Samples D and E with $Ir_{22}Mn_{78}$ capping and under layers, respectively), Ir/Co/Pt (Sample F with Ir capping layer) structures for the another Co layer interfaces in the synthetic AFM systems. The samples consisting of [W capping layers]/Co/[Pt/Ir-multilayer] heavy metal (HM) (Sample G) and [$Ir_{22}Mn_{78}$ capping layers]/Co/[Pt/Ir-multilayer] HM (Sample H) were also prepared in order to compare the effect of interfacial DM interaction acting on one Co layer (Samples G and H) and that acting on the Co layer in the synthetic AFM systems with two Co layers (Samples A and D). As shown in Table I, from here, the prepared samples are called "Sample A" - "Sample H". The $Ir_{22}Mn_{78}$ (1 nm) and $Ir_{22}Mn_{78}$ (2 nm) used in Samples D, E and H are paramagnetic at room temperature because the blocking temperature is lower than room temperature (Supplemental Material Note 1 [46]). In fact, an exchange bias magnetic field (H_{bias}) at room temperature is zero for Sample D with $Ir_{22}Mn_{78}$ (2 nm), whereas H_{bias} is not zero and is applied perpendicular to the film plane for Sample D with $Ir_{22}Mn_{78}$ (4 nm) as shown in Supplemental Material Note 1 [46]. Typical cross-sectional transmission electron microscope (TEM) images for Samples A and D and the results of x-ray diffraction (XRD) measurements using a standard Cu anode x-ray tube for Samples A−F are shown in Figs. 1(c), 1(d), and 1(e), respectively. These TEM results and the results of XRD measurements show that Co/[Pt/Ir/Pt]/Co/Ir, $Ir_{22}Mn_{78}$/Co/[Pt/Ir/Pt]/Co/Ir layers and Ir/Co/[Pt/Ir/Pt]/Co/$Ir_{22}Mn_{78}$/Ir have a face-centered-cubic structure with the (111) texture. The TEM images also show that the bottom Ta and W capping layers are amorphous and the top Ta is oxidized. The XRD peaks at around $2\theta = 38.5$ degrees for Sample D and $2\theta = 38.0$ degrees for Sample E in Fig. 1(e) would be originating from strained NaCl-type MgO (111) peaks. TEM result of Samples A and D also shows MgO layer has an amorphous and (111) textured NaCl-type

TABLE I. Sample structures (stacks) prepared in this study, values of H_{shift} which is related to the magnitude of the in-plane stray field and the field originating from the AFM interlayer exchange coupling from the Co layer applied DM interaction field (H_{DM}) to another Co layer, and magnitude of interlayer exchange coupling ($|J_{\text{ex}}|$). Field-free switching is observed in Samples A, B, D, and E.

Sample name	Structure of prepared films	Thickness (nm)		Field-free switching	H_{shift}(mT)	J_{ex}(mJ/m^2)	References
A	Ta(1)/MgO(1.5)/W(t_W)/ Co(t_{Co})/Pt(0.6)/Ir(0.5)/ Pt(0.6)/Co(t_{Co})/Ir(2)/Ta(2)	$t_W = 1.5, 1.0$	$t_{\text{Co}} = 0.9, 1.1, 1.3, 1.5, 1.7, 1.9, 2.1$	Yes	−37	0.16	This work
B	Ta(1)/MgO(1.5)/Ta(t_{Ta})/ Co(t_{Co})/Pt(0.6)/Ir(0.5)/ Pt(0.6)/Co(t_{Co})//Ir(2)/Ta(2)	$t_{\text{Ta}} = 1.0$	$t_{\text{Co}} = 0.9, 1.1, 1.3, 1.5, 1.7, 1.9, 2.1$	Yes	−6	0.17	This work
C	Ta(1)/MgO(1.5)/Mo(t_{Mo})/ Co(t_{Co})/Pt(0.6)/Ir(0.5)/Pt(0.6)/ Co(t_{Co})//Ir(2)/Ta(2)	$t_{\text{Mo}} = 1.0$	$t_{\text{Co}} = 0.9, 1.1, 1.3, 1.5, 1.7, 1.9, 2.1$	No	–	0.31	This work
D	Ta(1)/MgO(1.5)/Ir$_{22}$Mn$_{88}$(t_{IrMn})/ Co(t_{Co})/Pt(0.6)/Ir(0.5)/Pt(0.6)/ Co(t_{Co})//Ir(2)/Ta(2)	$t_{\text{IrMn}} = 2.0, 4.0$	$t_{\text{Co}} = 0.9, 1.1, 1.3, 1.5, 1.7, 1.9, 2.1$	Yes	−3	0.23	This work
E	Ta(1)/MgO(1.5)/Ir(0.5)/ Co(t_{Co})/Pt(0.6)/Ir(0.5)/Pt(0.6)/ Co(t_{Co})/Ir$_{22}$Mn$_{88}$(t_{IrMn})/Ir(2)/Ta(2)	$t_{\text{IrMn}} = 1.0$	$t_{\text{Co}} = 0.9, 1.1, 1.3, 1.5, 1.7, 1.9, 2.1$	Yes	+7	0.13	This work
F	Ta(1)/MgO(1.5)/Ir(t_{Ir})/ Co(t_{Co})/Pt(0.6)/Ir(0.5)/Pt(0.6)/ Co(t_{Co})/Ir(2)/Ta(2)	$t_{\text{Ir}} = 0.5$	$t_{\text{Co}} = 0.9, 1.1, 1.3, 1.5, 1.7, 1.9, 2.1$	No	–	0.32	[23]
G	Ta(1)/MgO(1.5)/W(t_W)/ Co(t_{Co})/[Pt(1.0)/Ir(0.8)]$_4$/Ta(2)	$t_W = 1.5$	$t_{\text{Co}} = 1.3$	No	–	–	This work
H	Ta(1)/MgO(1.5)/Ir$_{22}$Mn$_{88}$(t_{IrMn})/ Co(t_{Co})/[Pt(1.0)/Ir(0.8)]$_4$/Ta(2)	$t_{\text{IrMn}} = 2.0$	$t_{\text{Co}} = 1.2$	No	–	–	This work

structure, respectively. These TEM and XRD results are consistent with each other. The sputtering and device fabrication are done in a similar way to the Ref. [17]. The magnetization measurements were carried out by a vibrating sample magnetometer. As shown in Table I, we measured the magnetic properties by preparing the samples with different thicknesses of Co layers (t_{Co}) for Samples A–F. For the measurements of the electrical properties, we used the samples with $t_{\text{Co}} = 1.1$ nm in Samples A–F. The anomalous Hall effect (AHE) and current-induced magnetization switching were measured by the four-point probe method in a Hall cross at room temperature. The measurement configuration is sketched in Fig. 1(f). By rotating the samples, the external magnetic field was applied in any direction in the x-z plane to estimate the dampinglike SOT efficiency (ξ_{DL}). For the measurements of spin-Hall magnetoresistance (SMR), the current, which is less than equal to 5 μA, is passed through the devices in the x axis direction in Fig. 1(g), and an external magnetic field between −3 and +3 T is applied to both y- and z-axes directions by using the Quantum Design, Physical Properties Measurement System at 305 K.

III. RESULTS OF MAGNETIC AND ELECTRICAL PROPERTIES

A. Magnetic properties

Figures 2(a)–2(f) show the typical normalized out-of-plane and in-plane magnetization versus field (M-H) curves for Samples A−F with $t_{\text{Co}} = 1.1$ nm, respectively. As shown in Figs. 2(a)–2(f), the remanent magnetization in the out-of-plane direction at the external field $(H_{\text{ex}}) = 0$ mT is not zero except for Sample F. This indicates the existence of a dead layer at the Co interface. Corresponding AHE curves for Samples A–F are shown in Supplemental Material Note 2 [46]. The anomalous Hall resistivity in samples with Co/[Pt/Ir/Pt]/Co Synthetic AFM layers is expressed by $R_{xy} = 4\pi(R_{\text{S}}^{\text{top}}M_{\text{s}}^{\text{top}} + R_{\text{s}}^{\text{bot}}M_{\text{S}}^{\text{bot}})$, where $R_{\text{S}}^{\text{top}}$ and $R_{\text{S}}^{\text{bot}}$ are the anomalous Hall coefficient of top and bottom Co layers, and $M_{\text{S}}^{\text{top}}$ and $M_{\text{S}}^{\text{bot}}$ are the corresponding z-axis components of magnetization, respectively. The results of AHE curves are consistent with those of M-H curves shown in Figs. 2(a)–2(f). The magnitude of the antiferromagnetically exchange field (H_{exch}) is defined as an intermediate value of the magnetic field that transitions from the small magnetization state at around zero magnetic field to the saturated magnetization state, as shown in Supplemental Material Note 2 [46]. The magnitude of interlayer exchange coupling $|J_{\text{ex}}|$ can be evaluated using $|J_{\text{ex}}| = M_{\text{s}}\, t\, H_{\text{exch}}$ [47,48], where t is the thickness of the Co/Pt layers [20,21]. We show the magnitude of $|J_{\text{ex}}|$ in Table I. Figures 3(a) and 3(b) show the t_{Co} dependence of multiplication of saturation magnetization (M_{S}) and t_{Co} ($M_{\text{S}}t_{\text{Co}}$) and effective magnetic anisotropy energy ($K_{\text{eff}}\, t^*$) including the effects of $|J_{\text{ex}}|$ and H_{DM}, respectively. $K_{\text{eff}} = K_{\text{b}} - M_S^2/2\mu_0 + 2\text{K}_{\text{i}}/t^*$ and $t^* = t_{\text{Co}} - t_{\text{dead}}$, where K_{b} is the bulk crystalline anisotropy, K_{i} is the interfacial anisotropy and $(-M_S^2/2\mu_0)$ is the demagnetization, where these values are

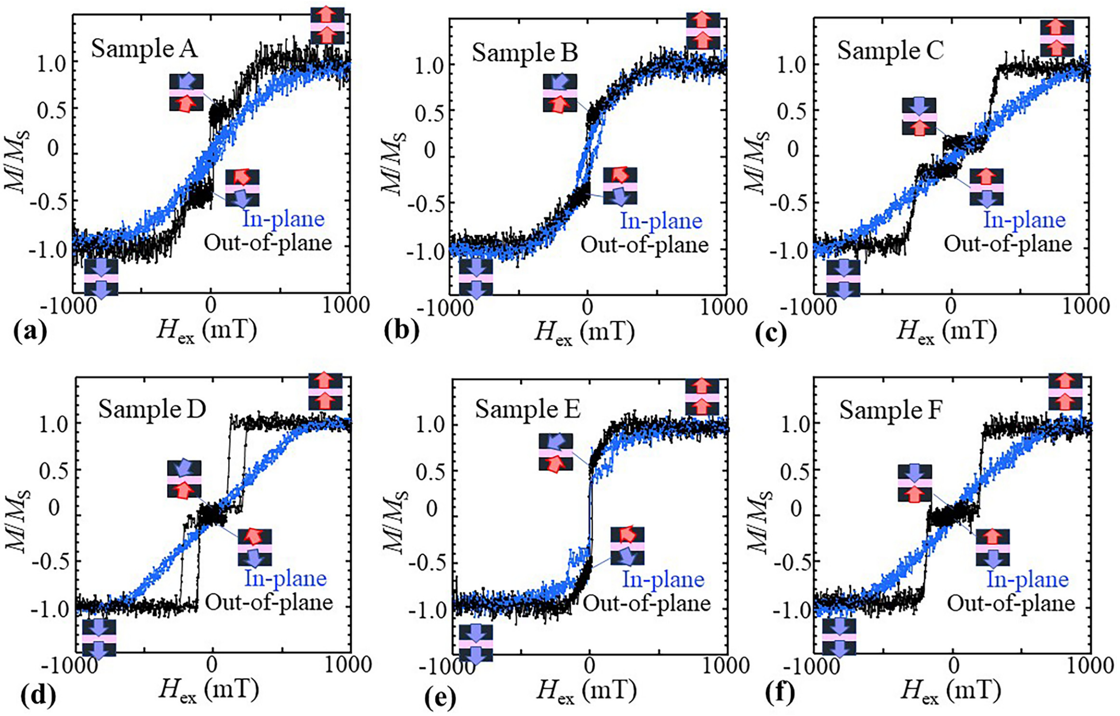

FIG. 2. (a)–(f) Normalized out-of-plane and in-plane magnetization versus field (*M-H*) curves for Samples A–F in Table I, respectively. The light red and light blue arrows in the dark blue color boxes in (a)–(f) indicate the corresponding magnetization direction of the top and bottom Co layers in the synthetic AFM layers for guides of the eyes.

including the effects of $|J_{ex}|$ and H_{DM}. μ_0 is the permeability of vacuum and t_{dead} is the magnetic dead layer thickness. As shown in Fig. 3(a), the *x*-axis intercept is 1.15, 1.17, 0.64, 0.40, 0.57, and 0.72 nm for Samples A–F, respectively. Assuming the values of t_{dead} at Ir/Co/Pt and Pt/Co/Ir interfaces in Sample F are the same, the dead layer thicknesses at each interface are estimated to be t_{dead} (Ir/Co/Pt) = 0.36 nm, t_{dead} (W/Co/Pt) = 0.79 nm, t_{dead} (Ta/Co/Pt) = 0.81 nm, t_{dead} (Mo/Co/Pt) = 0.28 nm, t_{dead} (IrMn/Co/Pt) = 0.04 nm and t_{dead} (Pt/Co/IrMn) = 0.21 nm. From the slope of the fitted lines in Fig. 3(a), the magnitudes of M_S are estimated to be 1.29×10^6 A/m, 1.24×10^6 A/m, 1.26×10^6 A/m, 1.13×10^6 A/m, 1.20×10^6 A/m, and 1.17×10^6 A/m for Samples A–F, respectively. From the *y* axis intercept in Fig. 3(b), the magnitudes of K_i are 0.73, 1.18, 2.07, 1.09, 0.81, and 1.55 [$\times 10^{-3}$ J/m^2] for Samples A–F, respectively. The estimated magnitude of K_i is larger for Ir/Co/Pt interfaces in Sample F than those for W/Co/Pt and Ta/Co/Pt interfaces in Samples A and B. Figure 3(b) also shows that the magnitudes of $K_{eff}\, t^*$ at the W/Co/Pt and Ta/Co/Pt interfaces are smaller than that at Ir/Co/Pt interfaces even in the thin t^* region in which perpendicular magnetization is observed. As shown later, *M-H* curves for Sample G with one Co layer and W/Co/Pt interfaces [Figs. 5(c)] indicate that the easy axis of the Co layer is tilted from out-of-plane direction. This tilting would be attributed to the H_{DM} induced at W/Co/Pt interfaces. Therefore, in the case of synthetic AFM structure with two Co layers and $|J_{ex}|$, magnetic properties such as the magnitudes of K_i and $K_{eff}\, t^*$ would also be influenced by the magnetization tilting due to the H_{DM} induced at W/Co/Pt and Ta/Co/Pt interfaces. In fact, there are reports [42,49,50] that the sign of DM interaction for W and Ta is known to have opposite in comparison with that for Pt and Ir, which difference depends on whether less-than-half-filled 5*d* states or more-than-half-filled 5*d* states. Therefore, the magnitudes of H_{DM} induced at W/Co/Pt, Ta/Co/Pt interfaces would be much larger than that at Ir/Co/Pt interfaces [22,40–45]. The observed smaller magnitudes of $K_{eff}\, t^*$ and K_i at the W/Co/Pt and Ta/Co/Pt interfaces compared to those at Ir/Co/Pt interfaces would be correlated to both magnitudes of $|J_{ex}|$ and H_{DM}. Therefore, the influence from these would be complex compared to that for Sample G with one Co layer. Further efforts are needed to confirm in more detail whether the magnitudes of K_i and $K_{eff}\, t^*$ correlate with the magnetization tilting angle due to the H_{DM}.

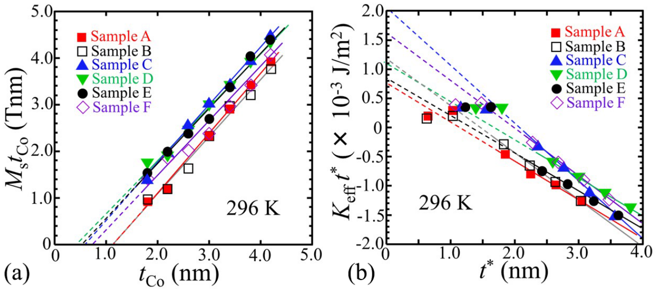

FIG. 3. (a) Co thickness (t_{Co}) dependence of multiplication of saturation magnetization (M_S) and t_{Co}, and (b) t^* ($= t_{Co} - t_{dead}$) dependence of effective magnetic anisotropy energy ($K_{eff}t^*$) including the effects of $|J_{ex}|$ and H_{DM} for Samples A–F. The solid lines are the results of linear fit using a least-squares method.

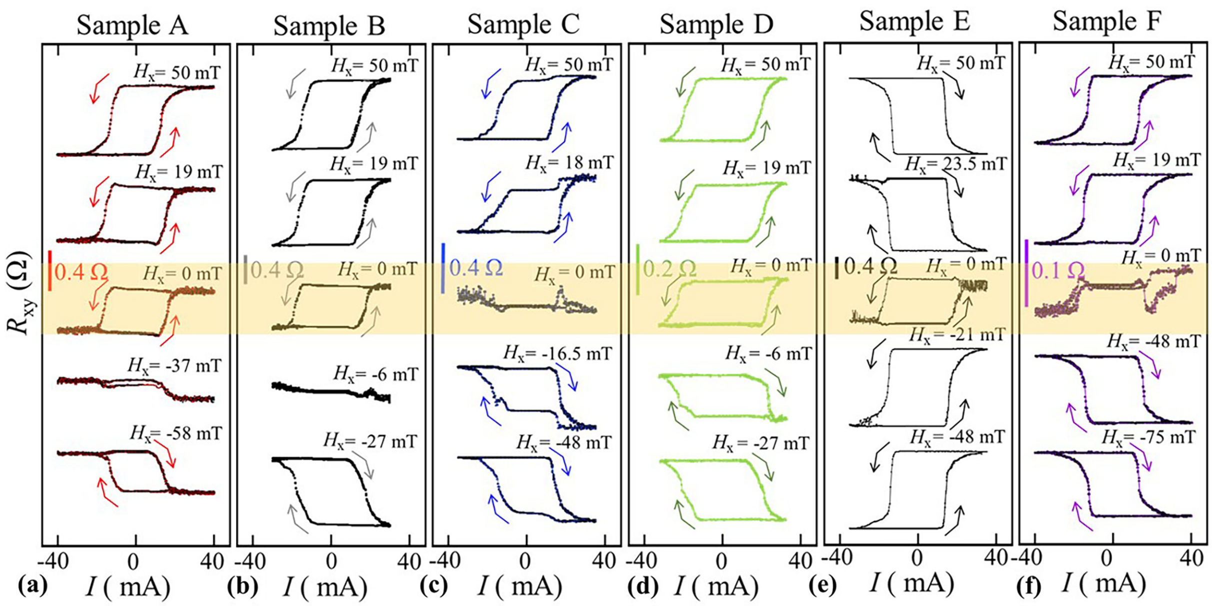

FIG. 4. Typical current-induced SOT switching for (a) Sample A with W (1 nm) capping layer, (b) Sample B with Ta (1 nm) capping layer, (c) Sample C with Mo (1 nm) capping layer, (d) Sample D with $Ir_{22}Mn_{78}$ (2 nm) capping layer, (e) Sample E with $Ir_{22}Mn_{78}$ (1 nm) underlayer, and (f) Sample F with Ir (0.5 nm) capping layer. Field-free switching is observed in Samples A, B, D, and E.

B. Current-induced magnetization switching properties

Next, we show the typical current-induced SOT switching in Figs. 4(a)–4(f) for Samples A (W capping layer), B (Ta capping layer), C (Mo capping layer), D ($Ir_{22}Mn_{78}$ capping layer), E ($Ir_{22}Mn_{78}$ underlayer), and F (Ir capping and underlayers), respectively. For this experiment, R_{xy} is recorded during the scanning of a pulse current (I) applied to the x axis of the Hall bars shown in Fig. 1(f) with an external magnetic field along the $\pm x$ direction (H_x). The pulse current width used in Figs. 4(a)–4(f) is 200 μsec. As shown in Figs. 4(a)–4(f), we observe field-free switching for Samples A (W capping layer), B (Ta capping layer), D ($Ir_{22}Mn_{78}$ capping layer), and E ($Ir_{22}Mn_{78}$ underlayer). When decreasing thickness of the W, Ta, and IrMn capping layers less than 0.5 nm, we could not observe field-free switching. The current-induced SOT switching shows opposite polarities under the $H_x < -37$ mT (clockwise switching direction) and $H_x > -37$ mT (anticlockwise switching direction) for Sample A, $H_x < -6$ mT (clockwise switching direction) and $H_x > -6$ mT (anticlockwise switching direction) for Sample B, $H_x < 0$ mT (clockwise switching direction) and $H_x > 0$ mT (anticlockwise switching direction) for Sample C, and $H_x < -3$ mT (clockwise switching direction) and $H_x > -3$ mT (anticlockwise switching direction) for Sample D, $H_x < +7$ mT (anticlockwise switching direction) and $H_x > +7$ mT (clockwise switching direction) for Sample E, and $H_x < 0$ mT (clockwise switching direction) and $H_x > 0$ mT (anticlockwise switching direction) for Sample F. In Samples D and E, clockwise and anticlockwise switching directions are opposite for the H_x. This is simply because the stack structures of Samples D and E are upside down. The values of $H_{\mathrm{shift}} = -37$, -6, -3, and $+7$ mT would be related to the magnitude of the in-plane stray field and the field originating from the AFM interlayer exchange coupling from the Co layer applied H_{DM} to another Co layer, as discussed later. The magnitude of H_{shift} for all samples with various capping layers is summarized in Table I. As shown in Figs. 4(c) and 4(f), no field-free switching was observed for the Mo-capping structure (Sample C) as well as for the Ir-capping structure (Sample F). As described before, the magnitude and sign of H_{DM} at Ir/Co and Co/Pt interfaces are similar and opposite, respectively [22,40–45], therefore, the H_{DM} applied to the Co layer with Ir/Co/Pt interfaces would be canceled and very small. Therefore, the H_{DM} applied to the Co layer with Mo/Co/Pt interfaces might also be canceled and very small. As described before, the sign of DM interaction for W and Ta is known to have opposite in comparison with that for Pt and Ir [42,49,50], which difference depends on whether less-than-half-filled $5d$ states or more-than-half-filled $5d$ states. Our results also show that sign of H_{DM} for W/Co/Pt and Ta/Co/Pt is the same as that for $Ir_{22}Mn_{78}$/Co/Pt. As shown above and Figs. 4(a)–4(f), by applying H_{DM} to one Co layer in the synthetic AFM systems with two Co layers, we succeed in observing a simple shift of SOT switching with respect to the external magnetic field, which would be easy to use in applications.

To confirm the role of H_{DM}, we measured M-H curves and prepared the Hall bar devices with one Co layer in [W-cap]/Co/[Pt/Ir-multilayer HM] (Sample G) and [$Ir_{22}Mn_{78}$-cap]/Co/[Pt/Ir-multilayer HM] (Sample H) [Table I and Figs. 5(a) and 5(b)]. Figures 5(c) and 5(d) show the normalized out-of-plane and in-plane M-H curves for Samples G and H, respectively. The light red and light blue arrows in the dark blue color boxes in Figs. 5(c) and 5(d) indicate the corresponding magnetization direction of the Co layer in Samples G and H. As shown in Figs. 5(c) and 5(d), the remanent magnetization in the out-of-plane direction at the zero external

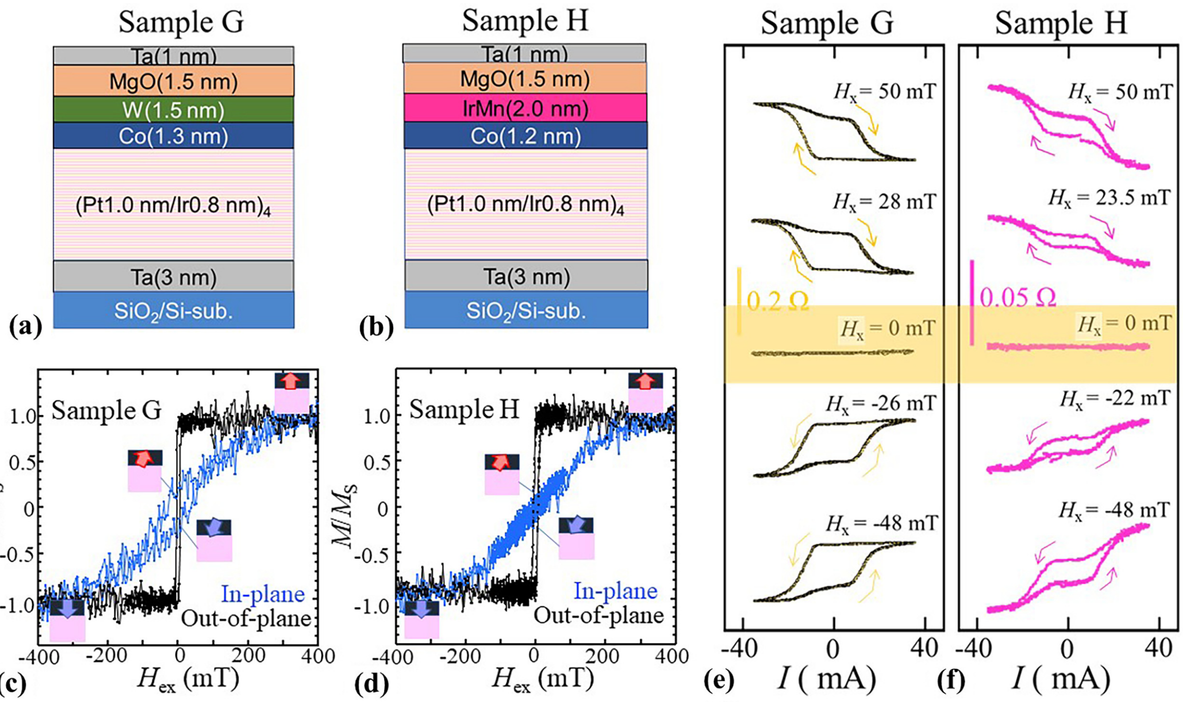

FIG. 5. (a), (b) Schematic of prepared film structures for Samples E and F in Table I, respectively. (c), (d) Normalized out-of-plane and in-plane *M-H* curves for Samples E and F, respectively. Typical current-induced SOT switching for (e) Sample E with W (1.5 nm) capping layer and (f) Sample F with $Ir_{22}Mn_{78}$ (2 nm) capping layer.

field ($H_{ex} = 0$ mT) is decreased from 1.0. These results indicate that the easy axis of Co layers in Samples G and H is tilted from out-of-plane direction. This tilting would be attributed to the H_{DM} induced at W/Co/Pt and $Ir_{22}Mn_{78}$/Co/Pt interfaces. Thus, we confirmed induced DM interaction for Samples G and H with one Co layer. Corresponding AHE curves for Samples G and H are shown in Supplemental Material Note 3 [46]. The results of AHE curves are consistent with those of *M-H* curves shown in Figs. 5(c) and 5(d).

Figures 5(e) and 5(f) show the results of current-induced SOT switching for Samples G (W capping layer) and H ($Ir_{22}Mn_{78}$ capping layer), respectively. For this experiment, R_{xy} is recorded during the scanning of a pulse I applied to the x axis of the Hall bars shown in Fig. 1(f). The pulse current width is 200 µsec. As shown in Figs. 5(e) and 5(f), the current-induced SOT switching shows opposite polarities under the $H_x > 0$ mT (clockwise switching direction) and $H_x < 0$ mT (anticlockwise switching direction) for Samples G and H. Thus, we did not observe field-free switching for Samples G and H. These results indicate that the structure of synthetic AFM layers is crucial for observing field-free switching in the case of the use of interfacial DM interaction. We think that the cause for observing field-free switching is related to the H_{shift} from the Co layer applied H_{DM} to another Co layer, as discussed later.

C. Estimation of spin-orbit torque efficiency ξ_{DL}

In order to estimate SOT efficiency (charge-to-spin conversion efficiency) in synthetic AFM system with various capping and underlayer, we record the R_{xy} when a fixed H_{ex} is rotating in *x-z* plane shown in Fig. 1(f) [22,28] for Samples A–F. Since the resistivity of the thin W and Ta layers is nearly an order of magnitude larger than the conducting layers, current flow into these layers is neglected in all samples. It has been reported that the magnitude of the dampinglike spin-orbit torque efficiency of paramagnetic IrMn is negligibly small [51]. Therefore, we thought that the influence of the capping layer and the underlayer such as W, Ta, and IrMn on current induced SOT switching is small compared to that of the conducting Co/Pt/Ir/Pt/Co layers in the synthetic AFM system. Figs. 6(a)–6(f) show the typical R_{xy} versus φ curves between $-30 < \varphi < 280$ degrees for Samples A–F, respectively. These curves are measured at $H_{ex} = 250$ mT and $I = \pm 10$ mA. As shown in Figs. 6(a)–6(f), switching is observed at around $\varphi = 0$ and $\varphi = 180$ degrees for all samples. Because the magnetization switching is occurred by a combination of the z component of the external magnetic field and the SOT effect, the opposite horizontal angle shift ($\Delta\varphi$) for the positive and negative current in the R_{xy} versus φ curves is observed as shown in Figs. 6(a)–6(f). The magnitudes of the shift of angle $\Delta\varphi$ are 2.7, 3.7, 9.0, 5.7, 3.4, and 12.1 degrees for Samples A–F at $H_{ex} = 250$ mT, respectively. When the rotating angle φ is small, the z component of the magnetic field $H_z = H_{ex} \sin\varphi \approx \varphi H_{ex}$, so, SOT effective magnetic field (H_{eff}) is estimated using $H_{eff} = H_{ex}\ \Delta\varphi$. Figure 7(a) shows the efficiency of effective field $\chi = H_{eff}/J$ as a function of H_{ex} for Samples A-F, where J is a current density during measurement. The magnitude of χ is related to the dampinglike SOT efficiency ($\xi_{DL} = T_{int}\ \theta_{SH}$), [22,28].

$$\xi_{DL} = \frac{8\chi e\mu_0 M_s t}{h\cos(\beta)}, \qquad (1)$$

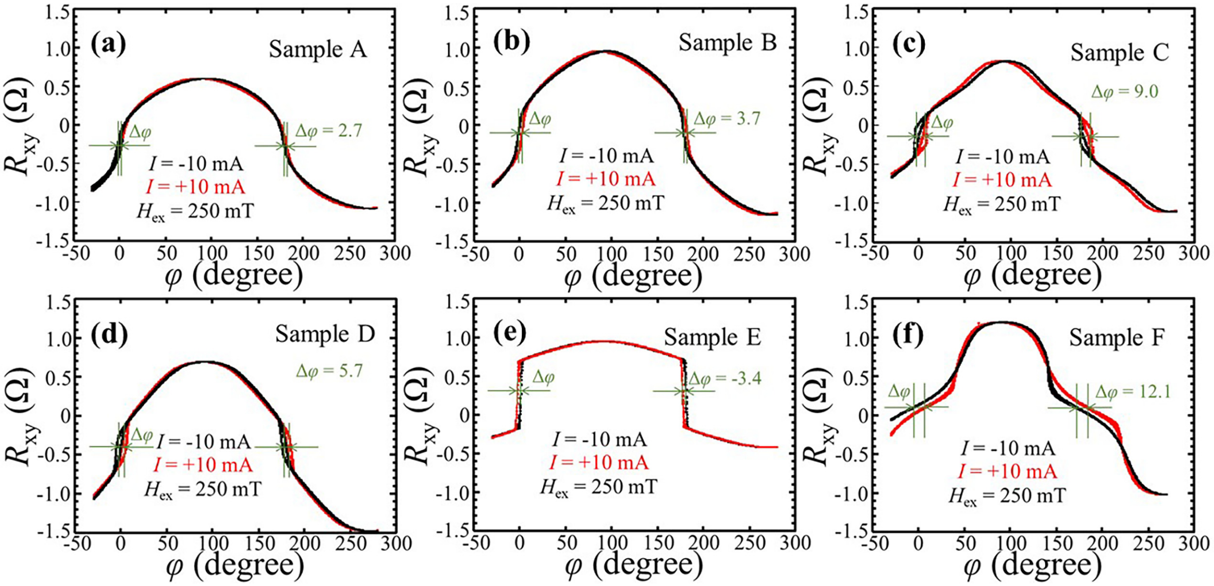

FIG. 6. Anomalous Hall curves measured when rotating an external magnetic field of 250 mT in xz plane of Fig. 1(f) with current $I = \pm 10$ mA for (a) Sample A with W capping layer, (b) Sample B with Ta capping layer, (c) Sample C with Mo capping layer, (d) Sample D with $\mathrm{Ir_{22}Mn_{78}}$ capping layer, (e) Sample E with $\mathrm{Ir_{22}Mn_{78}}$ underlayer, and (f) Sample F with Ir capping layer.

where T_{int} (<1), e, t, h, and μ_0 are interfacial spin transparency, elementary charge, thickness of the ferromagnetic layer, Plank constant and permeability of vacuum, respectively. We assume the $\cos(\beta)$ value is equal to 1, and we used the maximum values of χ in Fig. 7(a) for the estimation of ξ_{DL} [22]. In the case of the ferromagnetic system with heavy metal/one ferromagnetic layer structure, χ increases with increasing H_{ex} and saturates at around $H_{\mathrm{ex}} \approx 500$ mT [22]. The saturation behavior of χ indicates that the angle (β) between the central moment direction of the domain wall and the current direction become zero in the high H_{ex} region as discussed in Refs. [22,28]. On the other hand, the value of χ has a maximum in the low H_{ex} region and decreases with increasing H_{ex} in the case of a synthetic AFM system as shown in Fig. 7(a). This is because the spins of antiferromagnetic coupled Co layers in the synthetic AFM layers rotate together ferromagnetically in the direction of H_{ex} in the high H_{ex} region, and the efficiency of effective field χ decreases in the high H_{ex} region. The synthetic AFM systems with relatively large J_{ex} tend to have a maximum in χ at the high H_{ex} region and the maximum position of χ in the synthetic AFM systems would be correlated to the strength of J_{ex} as discussed in Ref. [23]. Therefore, because the angle (β) between the current direction and the central moment direction of the domain wall in a Co layer of synthetic AFM layers may not be parallel, the estimated value of ξ_{DL} in the synthetic AFM system would be the minimum value. For this estimation, we used $t = 1.1$ nm for the estimation of ξ_{DL}, because no significant increase in thermal stability factor [22] is observed for all samples. Figure 7(b) shows the dependence of ξ_{DL} on the magnitude of $|J_{\mathrm{ex}}|$. As shown in Fig. 7(b), the magnitude of ξ_{DL} for all samples is larger than ξ_{DL} of Pt HM layer ($\xi_{\mathrm{DL}} \sim 6$–10%) [22,52–55] and increases with increasing $|J_{\mathrm{ex}}|$. This trend of the correlation between $|J_{\mathrm{ex}}|$ and ξ_{DL} is consistent with previous result [23].

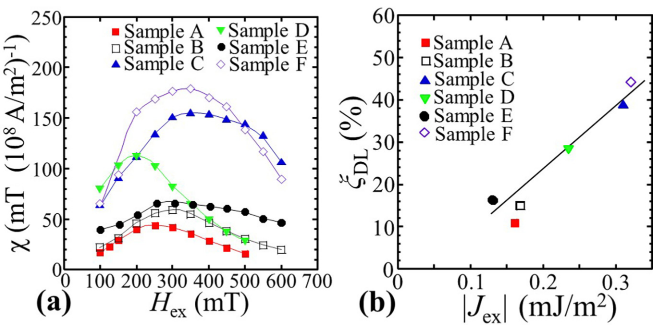

FIG. 7. (a) Efficiency of effective field $\chi = H_{\mathrm{eff}}/J$ as a function of the H_{ex} for Samples A–F. (b) Estimated dampinglike SOT efficiency (ξ_{DL}) as a function of $|J_{\mathrm{ex}}|$ for Samples A–F. The solid line in (b) is a result of linear fit using a least-squares method.

D. Spin Hall magnetoresistance

To confirm the degree of spin accumulation in the synthetic AFM systems, we measured SMR for Samples A–F. Figures 8(a)–8(f) show the longitudinal resistance (R_{xx}) versus H_{ex} measured at 305 K for Samples A–F, respectively. As shown in Figs. 8(a)–8(f), the magnitude of R_{xx} for the antiferromagnetically coupled Co state ($H_{\mathrm{ex}} \sim 0$ T) in synthetic AFM system [R_{xx} ($H_{\mathrm{ex}} \sim 0$ T)] is largest compared to that for the ferromagnetically aligned Co states [R_{xx} ($H_{\mathrm{ex}}^{z\text{-axis}} = \pm 3$ T), R_{xx} ($H_{\mathrm{ex}}^{y\text{-axis}} = \pm 3$ T)] in all SMR curves, whereas in general ferromagnet/heavy metal systems, when H_{ex} between -3 and $+3$ T is applied, the magnitude of R_{xx} ($H_{\mathrm{ex}}^{z\text{-axis}} = \pm 3$ T) has the largest value [17–20,56], where the $H_{\mathrm{ex}}^{y\text{-axis}}$ and $H_{\mathrm{ex}}^{z\text{-axis}}$ indicate that H_{ex} is applied to parallel to the y axis and z axis,

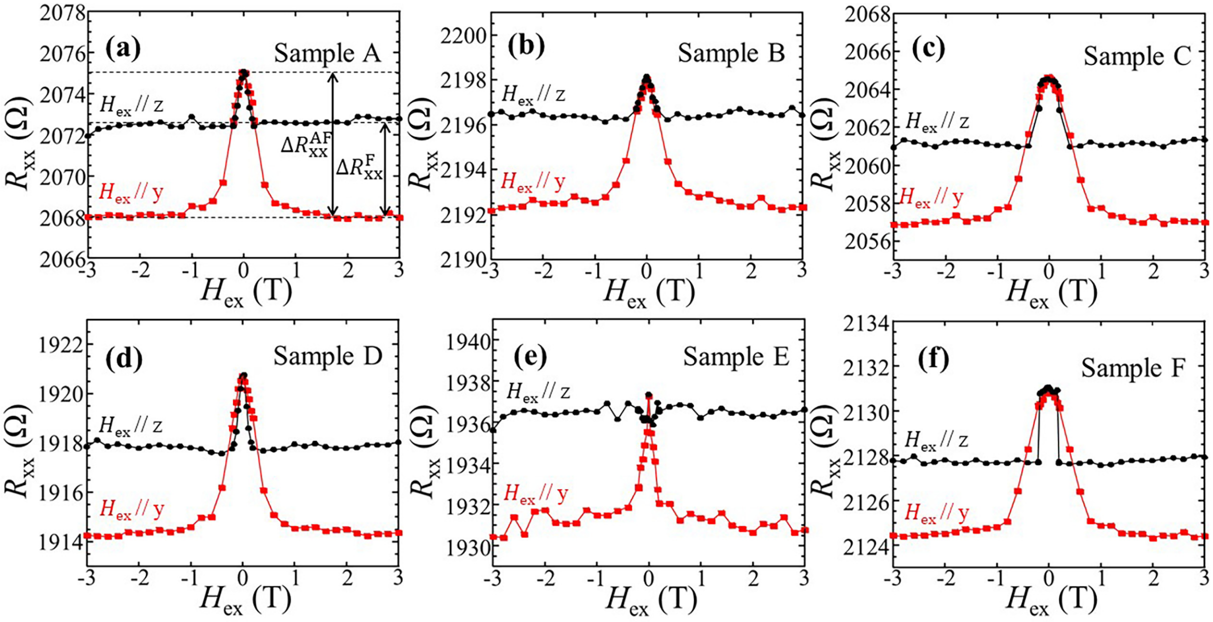

FIG. 8. (a)–(f) Typical longitudinal resistance R_{xx} versus external magnetic field H_{ex} oriented along the y axis (red closed symbols) and z axis (black closed symbols) measured at 305 K for Samples A–F, respectively.

respectively. These peculiar SMR curves observed in Figs. 8(a)–8(f) for synthetic AFM systems mean that the spin current flowing in the [Pt/Ir/Pt] spacer layer is absorbed more for the antiferromagnetic Co magnetization configuration compared to the ferromagnetic Co magnetization configuration. As shown in Fig. 8(a) and below, we defined the ΔR_{xx}^{AFM}, ΔR_{xx}^{F}, SMR^{AFM}, and SMR^{F}:

$$\Delta R_{xx}^{AFM} = R_{xx}(H_{ex} = 0\ \text{T}) - R_{xx}\left(H_{ex}^{y\text{-axis}} = \pm 3\ \text{T}\right), \tag{2}$$

$$\Delta R_{xx}^{F} = R_{xx}\left(H_{ex}^{Z\text{-axis}} = \pm 3\ \text{T}\right) - R_{xx}\left(H_{ex}^{y\text{-axis}} = \pm 3\ \text{T}\right), \tag{3}$$

$$\text{SMR}^{AFM} = \frac{\Delta R_{xx}^{AFM}}{R_{xx}\ (H_{ex} = 0\ \text{T})}, \tag{4}$$

$$\text{SMR}^{F} = \frac{\Delta R_{xx}^{F}}{R_{xx}\ (H_{ex} = 0\ \text{T})}. \tag{5}$$

Figure 9 shows the plots of SMR^{AFM}, SMR^{F}, and the ratio of $\text{SMR}^{AFM}/\text{SMR}^{F}$ as a function of $|J_{ex}|$ for Samples A–F. As shown in Fig. 9, we observed an increase in the ratio of $\text{SMR}^{AFM}/\text{SMR}^{F}$ with increasing $|J_{ex}|$. The magnitude of both SMR^{AFM} and SMR^{F} appears to decrease slightly with increasing $|J_{ex}|$. In order to confirm these trends are correct, we also measured SMR for the devices with the structures of [Ir capping layer]/Co(1.1)/Pt(0.6)/Ir(t_{Ir})/Pt(0.6)/Co(1.1)/[Ir underlayer]/Ta/thermal oxidized Si substrate previously prepared for the investigation of the correlation between $|J_{ex}|$ and ξ_{DL} [23]. The devices with $t_{Ir} = 0.5$, 0.52, 0.56, 0.58, and 0.6 nm have $|J_{ex}| = 0.32$, 0.25, 0.16, 0.14, and $0.026\ \text{mJ/m}^2$, respectively [23]. The observed results are shown in Supplemental Material Note 4 [46]. As shown in Supplemental Material Note 4 [46], consistent results, that is, peculiar SMR curves and the same trends for the SMR^{AFM}, SMR^{F}, and the ratio of $\text{SMR}^{AFM}/\text{SMR}^{F}$ as a function of $|J_{ex}|$ are observed. The SMR^{AFM} is given by [17–20,56,57]

$$\text{SMR}^{AFM} \sim \theta_{SH}^2 \frac{\lambda_S}{t} \frac{\tanh\left(t/2\lambda_S\right)}{1+\xi}\left[1 - \frac{1}{\cosh\left(t/\lambda_S\right)}\right], \tag{6}$$

where $\xi \equiv \frac{\rho_{Pt-Ir} t_{Co}}{\rho_{Co} t}$, and θ_{SH}, λ_S, t, and t_{Co} are spin Hall angle, spin diffusion length, the thicknesses of the [Pt/Ir/Pt] spacer, and the Co layers, respectively. Usually, θ_{SH}, and λ_S can be determined by fitting this equation by changing the film thickness of HM, however, it is difficult to determine these parameters by the fitting in the case of synthetic AFM systems because the magnitude and sign of J_{ex} changes as the

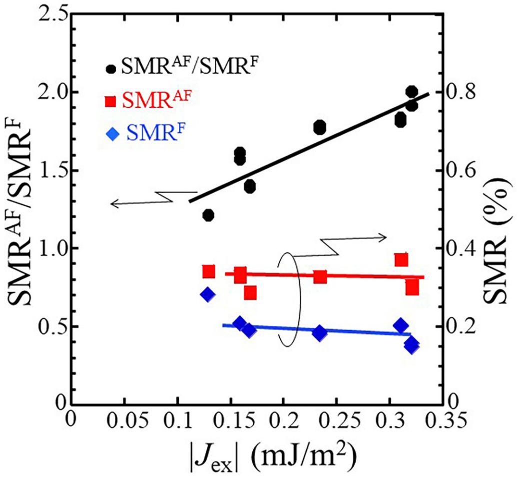

FIG. 9. Plots of SMR^{AFM}, SMR^{F} defined in Eqs. (4) and (5), and the ratio of $\text{SMR}^{AFM}/\text{SMR}^{F}$ as a function of $|J_{ex}|$ for Samples A–F.

HM film thickness changes. However, as described before, the results shown in Fig. 9 indicate that the enhancement of spin absorption in antiferromagnetically arranged configuration compared to that in ferromagnetically arranged configuration and the degree of enhancement increases with increasing $|J_{\mathrm{ex}}|$, which would be one of the reasons for observing enhancement of spin Hall angle with increasing $|J_{\mathrm{ex}}|$ [23] in the synthetic AFM system. As discussed above, both spins separated vertically by the SHE are found to be absorbed in large quantities, and both vertically separated and absorbed spins could be used for the SOT switching in the case of antiferromagnetically arranged synthetic AFM system. We compare the magnitude of the $\mathrm{SMR}^{\mathrm{AFM}}$ and the ratio of $\mathrm{SMR}^{\mathrm{AFM}}/\mathrm{SMR}^{\mathrm{F}}$ in the synthetic AFM systems with Ir-cap (Sample F) and $\mathrm{Ir}_{22}\mathrm{Mn}_{78}$-cap (Sample D), $\mathrm{SMR}^{\mathrm{AFM}}$ (Sample F) $= 0.31\%$, $\mathrm{SMR}^{\mathrm{AFM}}$ (Sample D) $= 0.33\%$, $\mathrm{SMR}^{\mathrm{AFM}}/\mathrm{SMR}^{\mathrm{F}}$ (Sample F) $= 1.95$, $\mathrm{SMR}^{\mathrm{AFM}}/\mathrm{SMR}^{\mathrm{F}}$ (Sample D) $= 1.78$. These differences between Ir-cap (Sample F) and $\mathrm{Ir}_{22}\mathrm{Mn}_{78}$-cap (Sample D) are very small compared to the estimated differences of ξ_{DL} for Sample F with Ir-cap ($\xi_{\mathrm{DL}} = 44.3\%$) and Sample D with $\mathrm{Ir}_{22}\mathrm{Mn}_{78}$-cap ($\xi_{\mathrm{DL}} = 28.1\%$). Therefore, as described before, ξ_{DL} estimated in Sample D with $\mathrm{Ir}_{22}\mathrm{Mn}_{78}$-cap might be much larger than estimated value of 28.1%, because the χ for Sample D has a maximum at relatively small H_{ex} value ($H_{\mathrm{ex}} = 200$ mT) as shown in Fig. 7(a). Thus, we succeed in simultaneously achieving field-free switching and high SOT efficiency using the $\mathrm{Ir}_{22}\mathrm{M}_{78}$-cap layer. On the other hand, in the case of Sample E ($\mathrm{Ir}_{22}\mathrm{Mn}_{78}$ underlayer), $\mathrm{SMR}^{\mathrm{AFM}}$ (Sample E) $= 0.34\%$, $\mathrm{SMR}^{\mathrm{AFM}}/\mathrm{SMR}^{\mathrm{F}}$ (Sample F) $= 1.22$, and we cannot observe the large enhancement for antiferromagnetically arranged synthetic AFM system comparing to that in the ferromagnetically arranged system. This would be due to the large magnitude of H_{DM} in the case of $\mathrm{Ir}_{22}\mathrm{Mn}_{78}$ underlayer (Sample E) and/or decrease of the magnitude of K_{i} observed in Fig. 3(b). There is a report [31] that the DM interaction is larger when interfacial mixing and roughness are small. This report [31] might indicate that in the case of $\mathrm{Ir}_{22}\mathrm{Mn}_{78}$ (1 nm) underlayer, interfacial mixing and roughness are small compared to the case of $\mathrm{Ir}_{22}\mathrm{Mn}_{78}$ (2 nm) capping layer. To observe the large magnitude of the ratio of $\mathrm{SMR}^{\mathrm{AFM}}/\mathrm{SMR}^{\mathrm{F}}$, that is, to observe large enhancement of spin absorption for antiferromagnetically arranged configuration compared to that in ferromagnetically arranged configuration in the case of $\mathrm{Ir}_{22}\mathrm{Mn}_{78}$ underlayer, we should decrease the magnitude of H_{DM} and increase the magnitude of K_{i} in $\mathrm{Pt/Co/Ir}_{22}\mathrm{Mn}_{78}$ underlayer.

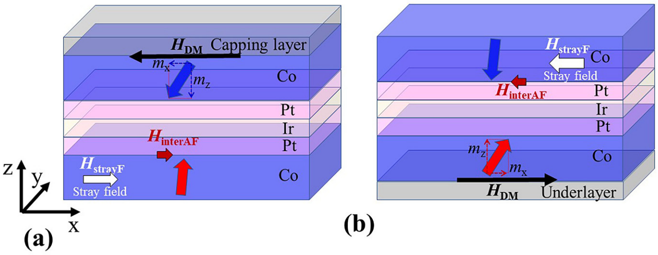

FIG. 10. Schematic diagrams of the model of field-free switching for the synthetic AFM systems with (a) W, Ta, $\mathrm{Ir}_{22}\mathrm{Mn}_{78}$ capping layers and (b) $\mathrm{Ir}_{22}\mathrm{Mn}_{78}$ underlayer.

IV. DISCUSSION

We discuss the origin of the field-free-switching observed in the synthetic AFM structure using the DM interaction. As described before, there are two kinds of DM interactions: interfacial DM [36,38,39] and interlayer DM [35,37] interactions. To utilize interlayer DM interaction for observing a field-free switching, a wedge structure in the film [34] is necessary for obtaining a 90-degree interlayer exchange coupling (interlayer DM interaction) between ferromagnetic layers. In our case, Samples A–H do not have a wedge structure because all samples were deposited on rotating substrates. Therefore, the present results would be attributed to interfacial DM interaction. There is a report that Néel's orange peel coupling through rough ferromagnetic interfaces also induces a 90° interlayer exchange coupling [58]. However, our prepared films have flat interfaces as shown in Figs. 1(c), 1(d), and Supplemental Material Note 5 [46]. Supplemental Material Note 5 [46] shows the result of energy dispersive x-ray spectroscopy of W in the cross-sectional TEM image for Sample A. The result shows that the 1 nm W capping layer on the Co layer in the synthetic AFM system is flat, so there is no orange peel interface in our systems. As shown in Figs. 4 and 5, field-free switching is observed in the synthetic AFM systems with W, Ta, $\mathrm{Ir}_{22}\mathrm{Mn}_{78}$ capping layers or $\mathrm{Ir}_{22}\mathrm{Mn}_{78}$ underlayer, however, not in the simple Co/[Pt/Ir-multilayer HM] systems with W or $\mathrm{Ir}_{22}\mathrm{Mn}_{78}$ capping layers. These results indicate that field-free switching could not be observed simply by applying the H_{DM} to the ferromagnetic interface. Figures 10(a) and 10(b) show schematic diagrams of the model of field-free switching for the synthetic AFM systems with W, Ta, $\mathrm{Ir}_{22}\mathrm{Mn}_{78}$ capping layers [Fig. 10(a)] and $\mathrm{Ir}_{22}\mathrm{Mn}_{78}$ underlayer [Fig. 10(b)]. The magnitude of H_{DM} is known to be tens to hundreds of mT [34,36,38,39,42,49,50]. As shown in Figs. 10(a) and 10(b), the easy axis of Co layers in the synthetic AFM system is tilted from the out-of-plane direction for Samples A, B, D, and E due to the H_{DM} induced at W/Co/Pt, Ta/Co/Pt, $\mathrm{Ir}_{22}\mathrm{Mn}_{78}$/Co/Pt and $\mathrm{Pt/Co/Ir}_{22}\mathrm{Mn}_{78}$ interfaces. As shown in Figs. 10(a) and 10(b), the magnetic moment of this tilted Co layer has m_x and m_z components. The component of m_x would apply a stray field (H_{strayF}) to another Co layer in the synthetic AFM system as discussed in Ref. [36]. The component of m_x would also apply a field originating from the AFM interlayer exchange coupling (H_{interAFM}) to another Co layer in the synthetic AFM system. We think that these fields are related to the H_{shift} described in Table I ($H_{\mathrm{shift}} = H_{\mathrm{strayF}} + H_{\mathrm{interAFM}}$), and would be the origin of field-free switching behavior shown in Fig. 4. As described before, LLG simulation [34] shows that the deterministic SOT critical switching field is mainly determined by the weaker one of the top and bottom H_{DM}. In Samples A–F, we designed the film structure in the synthetic AFM system with the Pt/Co/Ir multilayer (an Ir layer is used as either the capping or underlayer) because this multilayer has a very small DM interaction magnitude [22] as described before. Therefore, the Co in the Pt/Co/Ir layers to which the H_{shift} is applied would determine the critical switching field of the synthetic AFM system.

Considering the application to SOT-MRAM, a magnetic tunnel junction (MTJ) must be attached on the wiring of the synthetic AFM structure shown in Figs. 10(a) and 10(b) [20–22]. However, the capping layer insertion between the synthetic AFM layer and the MTJ would be not preferable to control the magnetization direction of the storage layer (free layer) in the MTJ by utilizing the exchange interaction between the storage and the synthetic AFM layer [20–22]. Therefore, a synthetic AFM system with an underlayer shown in Fig. 10(b) is preferable for realizing the application. As described before, we succeed in simultaneously achieving field-free switching and high SOT efficiency using the $\mathrm{Ir_{22}Mn_{78}}$ capping layer, however, we did not observe a large enhancement of ξ_{DL} in the case of $\mathrm{Ir_{22}Mn_{78}}$ underlayer. This would be due to the large magnitude of H_{DM} and/or decrease of the magnitude of K_{i} observed in Fig. 3(b) in the case of $\mathrm{Ir_{22}Mn_{78}}$ underlayer compared to that in $\mathrm{Ir_{22}Mn_{88}}$ capping layer as described before. To observe field-free switching and high SOT efficiency (large ξ_{DL}) simultaneously using the $\mathrm{Ir_{22}Mn_{78}}$ underlayer, we should decrease the magnitude of interfacial DM interaction and increase the magnitude of K_{i} in $\mathrm{Pt/Co/Ir_{22}Mn_{78}}$ underlayer. Increasing the concentration of Ir in the Ir-Mn underlayer would be one of solutions because we found that the magnitude of the DM interaction is very small for the Pt/Co/Ir layers [22] and a larger magnitude of K_{i} for the Pt/Co/Ir interfaces compared to the $\mathrm{Pt/Co/Ir_{22}Mn_{78}}$ interfaces. Because the stack structures of Sample D with $\mathrm{Ir_{22}Mn_{78}}$ capping layer and Sample E with an $\mathrm{Ir_{22}Mn_{78}}$ underlayer are upside down, and Ir-rich Ir-Mn has an fcc structure, therefore at least, we would be able to get the same properties between synthetic AFM systems with an $\mathrm{Ir_{22}Mn_{78}}$ capping layer and Ir-Mn underlayer by optimizing the concentration and thickness of Ir-Mn underlayer. We believe that we would also be able to achieve field-free switching and a large value of ξ_{DL} simultaneously in the case of Ir-Mn underlayer. We should make more efforts to simultaneously achieve field-free switching and high SOT efficiency using the Ir-Mn underlayer.

V. SUMMARY

In summary, we have studied the possibility of simultaneous achievement of field-free switching and a large value of ξ_{DL} in perpendicularly magnetized synthetic AFM systems by introducing the interface DM interaction. We investigated the synthetic AFM system in which one Co layer has a weak DM interaction and the other Co layer has a relatively large DM interaction. We used the Pt/Co/Ir structure for the one Co layer interface with a weak DM interaction and W/Co/Pt, Ta/Co/Pt, Mo/Co/Pt, $\mathrm{Ir_{22}Mn_{78}/Co/Pt}$, Ir/Co/Pt structures for another Co layer interface in the synthetic AFM systems. As a result, we observed field-free switching for the synthetic AFM systems with W/Co/Pt, Ta/Co/Pt, and $\mathrm{Ir_{22}Mn_{78}/Co/Pt}$ structures for other Co layer interfaces. We succeed in observing simultaneous achievement of field-free switching and a large value of ξ_{DL} in a perpendicularly magnetized synthetic AFM system with $\mathrm{Ir_{22}Mn_{78}/Co/Pt}$ structure. We also found that the observed large ξ_{DL} is related to the enhancement of spin absorption in antiferromagnetic Co magnetization configuration in the synthetic AFM system compared to that in the ferromagnetic Co magnetization configuration and the degree of enhancement increases with increasing the magnitude of interlayer exchange coupling between Co layers in the synthetic AFM system. The design of the synthetic AFM film structures presented here will be useful for future nonvolatile high-speed memories and logic circuits using the SHE.

ACKNOWLEDGMENTS

This work was supported by the CIES Consortium, Ministry of Education, Culture, Sports, Science and Technology (MEXT) Initiative to Establish Next-generation Novel Integrated Circuits Centers (X-NICS) Grants No. JPJ011438 and Japan Society for the Promotion of Science (JSPS) KAKENHI (No. JP19H00844 and No. JP21K18189). The authors also thank T. Miyazaki for TEM observation.

---

[1] L. Liu, C.-F. Pai, Y. Li, H. W. Tseng, D. C. Ralph, and R. A. Buhrman, Science **336**, 555 (2012).

[2] G. Yu, P. Upadhyaya, Y. Fan, J. G. Alzate, W. Jiang, K. L. Wong, S. Takei, S. A. Bender, L.-T. Chang, Y. Jiang, M. Lang, J. Tang, Y. Wang, Y. Tserkovnyak, P. K. Amiri, and K. L. Wang, Nat. Nanotech. **9**, 548 (2014).

[3] W. Jiang, P. Upadhyaya, W. Zhang, G. Yu, M. B. Jungfleisch, F. Y. Fradin, J. E. Pearson, Y. Tserkovnyak, K. L. Wang, O. Heinonen, S. G. E. Velthuis, and A. Hoffmann, Science **349**, 283 (2015).

[4] P. P. J. Haazen, E. Mure, J. H. Franken, R. Lavrijsen, H. J. M. Swagten, and B. Koopmans, Nat. Mater. **12**, 299 (2013).

[5] A. Chernyshov, M. Overby, X. Liu, J. K. Furdyna, Y. Lyanda-Geller, and L. P. Rokhinson, Nat. Phys. **5**, 656 (2009).

[6] I. M. Miron, K. Garello, G. Gaudin, P.-J. Zermatten, M. V. Costache, S. Auffret, S. Bandiera, B. Rodmacq, A. Schuhl, and P. Gambardella, Nature (London) **476**, 189 (2011).

[7] J. Kim, J. Sinha, M. Hayashi, M. Yamanouchi, S. Fukami, T. Suzuki, S. Mitani, and H. Ohno, Nat. Mater. **12**, 240 (2013).

[8] S. Fukami, T. Anekawa, C. Zhang, and H. Ohno, Nat. Nanotech. **11**, 621 (2016).

[9] K. S. Lee, S. W. Lee, B. C. Min, and K. J. Lee, Appl. Phys. Lett. **104**, 072413 (2014).

[10] K. Garello, C. O. Avci, I. M. Miron, M. Baumgartner, A. Ghosh, S. Auffret, O. Boulle, G. Gaudin, and P. Gambardella, Appl. Phys. Lett. **105**, 212402 (2014).

[11] C. Zhang, S. Fukami, H. Sato, F. Matsukura, and H. Ohno, Appl. Phys. Lett. **107**, 012401 (2015).

[12] M. H. Nguyen, C. F. Pai, K. X. Nguyen, D. A. Muller, D. C. Ralph, and R. A. Buhrman, Appl. Phys. Lett. **106**, 222402 (2015).

[13] S. V. Aradhya, G. E. Rowlands, J. Oh, D. C. Ralph, and R. A. Buhrman, Nano Lett. **16**, 5987 (2016).

[14] M. Baumgartner, K. Garello, J. Mendil, C. O. Avci, E. Grimaldi, C. Murer, J. Feng, M. Gabureac, C. Stamm, Y. Acremann, S. Finizio, S. Wintz, J. Raabe, and P. Gambardella, Nat. Nanotech. **12**, 980 (2017).

[15] Y. Kato, Y. Saito, H. Yoda, T. Inokuchi, S. Shirotori, N. Shimomura, S. Oikawa, A. Tiwari, M. Ishikawa, M. Shimizu,

B. Altansargai, H. Sugiyama, K. Koi, Y. Ohsawa, and A. Kurobe, Phys. Rev. Appl. **10**, 044011 (2018).

[16] H. Honjo, T. V. A. Nguen, T. Watanabe, T. Nasuno, C. Zhang, T. Tanigawa, S. Miura, H. Inoue, M. Niwa, T. Yoshiduka, Y. Noguchi, M. Yasuhira, A. Tamakoshi, M. Natsui, Y. Ma, H. Koike, Y. Takahashi, K. Furuya, H. Shen, S. Fukami, H. Sato, S. Ikeda, T. Hanyu, H. Ohno, and T. Endoh, IEDM Tech. Dig. 28.5.1 (2019), doi:10.1109/IEDM19573.2019.8993443.

[17] Y. Saito, N. Tezuka, S. Ikeda, H. Sato, and T. Endoh, Appl. Phys. Exp. **12**, 053008 (2019).

[18] Y. Saito, N. Tezuka, S. Ikeda, H. Sato, and T. Endoh, AIP. Advances **9**, 125312 (2019).

[19] Y. Saito, N. Tezuka, S. Ikeda, and T. Endoh, Appl. Phys. Lett. **116**, 132401 (2020).

[20] Y. Saito, N. Tezuka, S. Ikeda, and T. Endoh, Phys. Rev. B **104**, 064439 (2021).

[21] Y. Saito, S. Ikeda, and T. Endoh, Appl. Phys. Lett. **119**, 142401 (2021).

[22] Y. Saito, S. Ikeda, and T. Endoh, Phys. Rev. B **105**, 054421 (2022).

[23] Y. Saito, S. Ikeda, and T. Endoh, Appl. Phys. Exp. **16**, 013002 (2023).

[24] S. Ikeda, K. Miura, H. Yamamoto, K. Mizunuma, H. D. Gan, M. Endo, S. Kanai, J. Hayakawa, F. Matsukura, and H. Ohno, Nat. Mater. **9**, 721 (2010).

[25] G. Y. Shi, C. H. Wan, Y. S. Chang, F. Li, X. J. Zhou, P. X. Zhang, J. W. Cai, X. F. Han, F. Pan, and C. Song, Phys. Rev. B **95**, 104435 (2017).

[26] Q. L.Ma, Y. F. Li, Y. S. Choi, W. C. Chen, S. J. Han, and C. L. Chien, Appl. Phys. Lett. **117**, 172403 (2020).

[27] Y. Ishikuro, M. Kawaguchi, T. Taniguchi, and M. Hayashi, Phys. Rev. B **101**, 014404 (2020).

[28] P. X. Zhang, L. Y. Liao, G. Y. Shi, R. Q. Zhang, H. Q. Wu, Y. Y. Wang, F. Pan, and C. Song, Phys. Rev. B **97**, 214403 (2018).

[29] L. Liu, X. T. Zhao, W. Liu, Y. H. Song, X. G. Zhao, and Z. D. Zhang, J. Phys. D **54**, 505003 (2021).

[30] R. Q. Zhang, G. Y. Shi, J. Su, Y. X. Shang, J. W. Cai, L. Y. Liao, F. Pan, and C. Song, Appl. Phys. Lett. **117**, 212403 (2020).

[31] R. Y. Chen, Q. R. Cui, L. Y. Liao, Y. M. Zhu, R. Q. Zhang, H. Bai, Y. J. Zhou, G. Z. Xing, F. Pan, H. X. Yang, and C. Song, Nat. Commun. **12**, 3113 (2021).

[32] J. W. Wei, X. Wang, B. S. Cui, C. Y. Guo, H. J. Xu, Y. Guang, Y. Q. Wang, X. M. Luo, C. H. Wan, J. F. Feng, H. X. Wei, G. Yin, X. F. Han, and G. Q. Yu, Adv. Funct. Mater. **32**, 2109455 (2022).

[33] H. Fan, M. Jin, Y. Luo, H. Yang, B. Wu, Z. Feng, Y. Zhuang, Z. Shao, C. Yu, H. Li, J. Wen, N. Wang, B. Liu, W. Li, and T. Zhou, Adv. Funct. Mater. **33**, 2211953 (2023).

[34] T. Zhou, X. Xie, X. Zhao, Y. Dong, J. Wang, W. Chen, Q. Huang, Q. Leng, L. Bai, Y. Chen, S. Yan, and Y. Tian, Phys. Rev. B **105**, 144434 (2022).

[35] W. He, C. Wan, C. Zheng, Y. Wang, X. Wang, T. Ma, Y. Wang, C. Guo, X. Luo, M. E. Stebliy, G. Yu, Y. Liu, A. V. Ognev, A. S. Samardak, and X. Han, Nano Lett. **22**, 6857 (2022).

[36] L. B. Zhu, X. G. Xu, M. X. Wang, K. K. Meng, Y. Wu, J. K. Chen, J. Miao, and Y. Jiang, Appl. Phys. Lett. **117**, 112401 (2020).

[37] H. Masuda, T. Seki, Y. Yamane, R. Modak, K. I. Uchida, J. Ieda, Y.-C. Lau, S. Fukami, and K. Takanashi, Phys. Rev. Appl. **17**, 054036 (2022).

[38] A. Fert, V. Cros, and J. Sampaio, Nat. Nanotech. **8**, 152 (2013).

[39] S.-H. Yang, K.-S. Ryu, and S. Parkin, Nat. Nanotech. **10**, 221 (2015).

[40] J. Han, A. Richardella, S. A. Siddiqui, J. Finley, N. Samarth, and L. Liu, Phys. Rev. Lett. **119**, 077702 (2017).

[41] K. S. Ryu, S. H. Yang, L. Thomas, and S. S. P. Parkin, Nat. Commun. **5**, 3910 (2014).

[42] K. Shahbazi, J.-V. Kim, H. T. Nembach, J. M. Shaw, A. Bischof, M. D. Rossell, V. Jeudy, T. A. Moore, and C. H. Marrows, Phys. Rev. B **99**, 094409 (2019).

[43] P. M. Shepley, H. Tunnicliffe, K. Shahbazi, G. Burnell, and T. A. Moore, Phys. Rev. B **97**, 134417 (2018).

[44] D. Khadka, S. Karayev, and S. X. Huang, J. Appl. Phys. **123**, 123905 (2018).

[45] N. H. Kim, J. Jung, J. Cho, D. S. Han, Y. X. Yin, J. S. Kim, H. J. M. Swagten, and C. Y. You, Appl. Phys. Lett. **108**, 142406 (2016).

[46] See Supplemental Material at http://link.aps.org/supplemental/10.1103/PhysRevB.108.024419 for Note 1. Temperature dependence of exchange bias magnetic field in synthetic AF layer consisting of [$Ir_{22}Mn_{78}$ capping layer]/Co/[Pt/Ir/Pt]/Co/[Ir underlayer]; Note 2. Magnetic properties in synthetic antiferromagnet with W, Ta, Mo, $Ir_{22}Mn_{78}$, Ir capping layers and $Ir_{22}Mn_{78}$ underlayer measured by the anomalous Hall effect; Note 3. Magnetic properties in the [W-capping layer]/Co/[Pt/Ir-multilayer HM] and [$Ir_{22}Mn_{78}$-capping layer]/Co/[Pt/Ir-multilayer HM] measured by the anomalous Hall effect; Note 4. Spin Hall magnetoresistance in the synthetic AF systems consisting of [Ir capping layer]/Co(1.1)/[Pt(0.6)/Ir(t_{Ir})/Pt(0.6)]/Co(1.1)/[Ir underlayer]/Ta structure ($t_{Ir} = 0.5$, 0.52, 0.56, 0.58 and 0.6 nm); Note 5. Energy dispersive x-ray spectroscopy of W in Sample A.

[47] P. J. H. Bloemen, H. W. van Kesteren, H. J. M. Swagten, and W. J. M. deJonge, Phys. Rev. B **50**, 13505 (1994).

[48] W. Folkerts, J. Magn. Magn. Mater. **94**, 302 (1991).

[49] N. Kato, M. Kawaguchi, Y.-C. Lau, T. Kikuchi, Y. Nakatani, and M. Hayashi, Phys. Rev. Lett. **122**, 257205 (2019).

[50] S. Emori, U. Bauer, S.-M. Ahn, E. Martinez, and G. S. D. Beach, Nat. Mater. **12**, 611 (2013).

[51] H. Reichlová, D. Kriegner, V. Holý, K. Olejník, V. Novák, M. Yamada, K. Miura, S. Ogawa, H. Takahashi, T. Jungwirth, and J. Wunderlich, Phys. Rev. B **92**, 165424 (2015).

[52] T. Fache, J. C. Rojas-Sanchez, L. Badie, S. Mangin, and S. Petit-Watelot, Phys Rev. B **102**, 064425 (2020).

[53] R. Ramaswamy, Y. Wang, M. Elyasi, M. Motapothula, T. Venkatesan, X. Qiu, and H. Yang, Phys Rev. Appl. **8**, 024034 (2017).

[54] M. Isasa, E. Villamor, L. E. Hueso, M. Gradhand, and F. Casanova, Phys Rev. B **91**, 024402 (2015).

[55] L. Wang, R. J. H. Wesselink, Y. Liu, Z. Yuan, K. Xia, and P. J. Kelly, Phys. Rev. Lett. **116**, 196602 (2016).

[56] J. Kim, P. Sheng, S. Takahashi, S. Mitani, and M. Hayashi, Phys. Rev. Lett. **116**, 097201 (2016).

[57] J. Liu, T. Ohkubo, S. Mitani, K. Hono, and M. Hayashi, Appl. Phys. Lett. **107**, 232408 (2015).

[58] J. C. S. Kools, W. Kula, D. Mauri, and T. Lin, J. Appl. Phys. **85**, 4466 (1999).